Active transport of cargo-carrying and interconnected chiral particles

Bhavesh Valecha, Hossein Vahid, Pietro Luigi Muzzeddu, Jens-Uwe Sommer, Abhinav Sharma

Angaben zur Veröffentlichung / Publication details:

Valecha, Bhavesh, Hossein Vahid, Pietro Luigi Muzzeddu, Jens-Uwe Sommer, and Abhinav Sharma. 2025. "Active transport of cargo-carrying and interconnected chiral particles." *Soft Matter* 21 (17): 3384–92. https://doi.org/10.1039/d5sm00170f.

Active transport of cargo-carrying and interconnected chiral particles†

Bhavesh Valecha,[a] Hossein Vahid,[b] Pietro Luigi Muzzeddu,[c] Jens-Uwe Sommer[bd] and Abhinav Sharma *[ab]

Directed motion up a concentration gradient is crucial for the survival and maintenance of numerous biological systems, such as sperms moving towards an egg during fertilization or ciliates moving towards a food source. In these systems, chirality—manifested as a rotational torque—plays a vital role in facilitating directed motion. While systematic studies of active molecules in activity gradients exist, the effect of chirality remains little studied. In this study, we examine the simplest case of a chiral active particle connected to a passive particle in a spatially varying activity field. We demonstrate that this minimal setup can exhibit rich emergent tactic behaviors, with the chiral torque serving as the tuning parameter. Notably, when the chiral torque is sufficiently large, even a small passive particle enables the system to display the desired accumulation behavior. Our results further show that in the dilute limit, this desired accumulation behavior persists despite the presence of excluded volume effects. Additionally, interconnected chiral active particles exhibit emergent chemotaxis beyond a critical chain length, with trimers and longer chains exhibiting strong accumulation at sufficiently high chiral torques. This study provides valuable insights into the design principles of hybrid bio-molecular devices of the future.

I. Introduction

Active matter systems represent a broad class of nonequilibrium systems that convert environmental energy into directed motion, enabling them to respond to external stimuli.[1–5] One of the most well-known forms of directed transport in such systems is chemotaxis, the ability of microorganisms like *Escherichia coli* to navigate chemical gradients.[6] Bacteria achieve this *via* a run-and-tumble strategy, adjusting their motion in response to nutrient gradients.[7,8] Synthetic analogs of chemotaxis, such as phoretic Janus colloids with catalytic coatings, have been experimentally realized, demonstrating self-propulsion in response to chemical gradients.[3,4]

To model chemotaxis theoretically, various approaches have been developed. Simple active Brownian particle (ABP) models[9] capture self-propulsion and persistence but typically lead to accumulation in low-fuel regions due to orthokinesis.[10–13] To overcome this limitation, explicit coupling to concentration gradients,[14–16] feedback mechanisms,[17–19] and external control *via* light or magnetic fields[20–22] have been proposed. It has also been demonstrated that the presence of torques aligning the self-propulsion of active particles, either parallel or anti-parallel to activity gradients, can suppress or enhance their tactic behavior, respectively.[23,24] More recently, alternative strategies have been devised, in which directed motion arises as an emergent property without external feedback. Examples include coupling an active particle to a passive particle,[25] active colloidal molecules with fixed orientations,[26] and chains of active particles.[27]

A relatively underexplored aspect of chemotactic transport is the role of chirality, which is ubiquitous in both biological locomotion and synthetic active systems. Chirality introduces an intrinsic rotational component to active motion, fundamentally altering transport properties.[28,29] Many biological microswimmers, such as bacteria,[30,31] sperm cells,[32,33] and flagellated algae,[34] exhibit helical or rotational swimming due to internal asymmetries. Advances in fabrication techniques have enabled the design of artificial chiral active particles, including colloidal spinners, magnetic rotors, and chiral granular particles, revealing novel transport properties.[35–38] Chirality has also been shown to suppress wall adhesion and give rise to surface currents,[39] induce phase separation,[40] generate spontaneous angular momentum in active crystals,[41] and break time-reversal symmetry leading to

[a] *Mathematisch-Naturwissenschaftlich-Technische Fakultät, Institut für Physik, Universität Augsburg, Universitätsstraße 1, 86159 Augsburg, Germany. E-mail: abhinav.sharma@uni-a.de*
[b] *Leibniz-Institut für Polymerforschung Dresden, Institut Theory der Polymere, 01069 Dresden, Germany*
[c] *Department of Biochemistry, University of Geneva, CH-1205 Geneva, Switzerland*
[d] *Institut für Theoretische Physik, Technische Universität Dresden, 01069 Dresden, Germany*

† Electronic supplementary information (ESI) available. See DOI: **https://doi.org/10.1039/d5sm00170f**

unidirectional wave propagation[42] and topologically protected excitations.[43]

In this work, we introduce chirality as a control parameter in active–passive transport. Our modeling closely follows the approach developed in our previous works.[25–27] We explore the impact of chirality on the accumulation of a passive cargo attached to an active chiral particle within an activity gradient. Our results demonstrate that chirality fundamentally changes the transition to chemotaxis: even when the passive particle is small, a sufficiently large chiral rotational torque enables preferential accumulation in high-activity regions. This is in contrast to previous findings, where a large passive particle was required to induce chemotaxis.[25] We further emphasize the robustness of the effect of chirality by performing simulations with excluded volume effects.

Additionally, chirality is naturally present in biological active systems composed of elongated structures, such as cytoskeletal filaments[44] and bacterial protofilaments.[45] We extend our analysis to chains of chiral active particles. We find that while monomers and dimers accumulate in the low-activity regions, trimers accumulate in the high-activity regions at high chirality levels. As chirality increases in longer chains, their accumulation in high-activity regions becomes more pronounced.

II. The model

We consider a two dimensional system of a chiral active particle and a passive particle interacting through a force $\boldsymbol{F}(\boldsymbol{r})$ in a spatially varying activity field (see Fig. 1). We model this active–passive composite with the overdamped Langevin dynamics given by the following coupled stochastic differential equations:

$$\frac{\mathrm{d}\boldsymbol{r}_1}{\mathrm{d}t} = \frac{1}{\gamma}\boldsymbol{F} + \frac{1}{\gamma}f_{\mathrm{s}}(\boldsymbol{r}_1)\boldsymbol{p} + \sqrt{\frac{2T}{\gamma}}\boldsymbol{\xi}_1(t), \tag{1a}$$

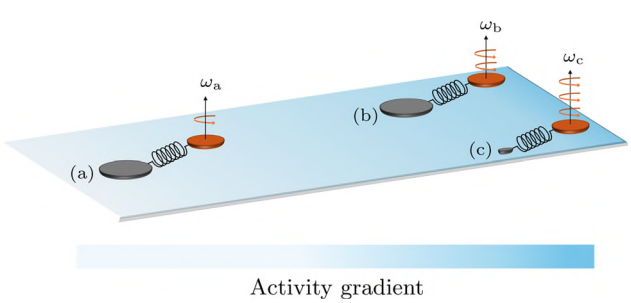

Fig. 1 Schematic of composites of a chiral active particle (orange) connected to a passive particle (grey) *via* a harmonic spring in a spatially varying activity field. The color bar below the schematic indicates the gradient in the activity field increasing in magnitude from left to right. The number of curved arrows indicates the strength of the chiral torque on the active particles about an axis perpendicular to the plane. Here, $\omega_{\mathrm{a}} < \omega_{\mathrm{b}} < \omega_{\mathrm{c}}$. Composites with a small torque on the active particle accumulate in low-activity regions (composite a), whereas those with a large chiral torque accumulate in high-activity regions (composite b). Furthermore, for a very large chiral torque on the active particle, a small passive particle is sufficient to facilitate accumulation in high-activity regions (composite c).

$$\frac{\mathrm{d}\theta}{\mathrm{d}t} = \omega + \sqrt{2D_{\mathrm{R}}}\eta(t), \tag{1b}$$

$$\frac{\mathrm{d}\boldsymbol{r}_2}{\mathrm{d}t} = -\frac{1}{q\gamma}\boldsymbol{F} + \sqrt{\frac{2T}{q\gamma}}\boldsymbol{\xi}_2(t). \tag{1c}$$

Here, $\boldsymbol{r}_1$ and $\boldsymbol{r}_2$ are the coordinates of the active and passive particle, respectively. The friction coefficient of the passive particle is q times that of the active particle, which is given by γ. For spherical active and passive particles in a Newtonian fluid, q is the ratio of their radii (sizes). The interaction force between the active and passive particles is modeled as a harmonic spring force $\boldsymbol{F} = -k(r - l_0)\hat{\boldsymbol{r}}$, where $\boldsymbol{r} = \boldsymbol{r}_1 - \boldsymbol{r}_2$, the spring constant is $k > 0$ and the rest length is l_0. The self-propulsion force of the active particle, whose magnitude is given by $f_{\mathrm{s}}(\boldsymbol{r}_1)$, is aligned with the rotational degree of freedom $\boldsymbol{p} = (\cos\theta, \sin\theta)$, where θ is the polar angle measured with respect to the x-axis. f_{s} will henceforth be referred to as the activity field. The active particle also experiences a constant chiral torque ω, in the direction perpendicular to the plane of motion, as well as rotational diffusion characterized by the diffusion coefficient D_{R}. The temperature T of the thermal bath is measured in units such that the Boltzmann constant k_{B} is set to unity. The stochastic terms $\boldsymbol{\xi}_1$, $\boldsymbol{\xi}_2$ and η are zero-mean independent Gaussian white noises, with correlations:

$$\begin{aligned} \langle \boldsymbol{\xi}_i(t) \otimes \boldsymbol{\xi}_i(t') \rangle &= \mathbb{1}\delta(t - t'), \\ \langle \eta(t)\eta(t') \rangle &= \delta(t - t'). \end{aligned} \tag{2}$$

with $\otimes$ denoting the outer product and $i \in \{1,2\}$.

The dynamics of the active–passive composite can be equivalently described by the collective coordinates, which we identify as the center of friction $\boldsymbol{R}$ and the bond coordinates $\boldsymbol{r}$, defined as:

$$\begin{aligned} \boldsymbol{R} &= \frac{1}{1+q}\boldsymbol{r}_1 + \frac{q}{1+q}\boldsymbol{r}_2, \\ \boldsymbol{r} &= \boldsymbol{r}_1 - \boldsymbol{r}_2. \end{aligned} \tag{3}$$

To analyze the spatial regions where the active–passive composite preferentially accumulates in the long-time limit, it is convenient to express the evolution equation for the one-time joint probability density $P(\boldsymbol{R},\boldsymbol{r},\theta,t) \equiv P$. Since the stochastic dynamics in eqn (1) is Markovian, this is simply given by the Fokker–Planck equation:[46]

$$\begin{aligned} \frac{\partial}{\partial t}P = &-\nabla_{\boldsymbol{R}} \cdot \left[\frac{1}{1+q}\frac{1}{\gamma}f_{\mathrm{s}}\boldsymbol{p}P - \frac{1}{1+q}\frac{T}{\gamma}\nabla_{\boldsymbol{R}}P\right] \\ &-\nabla_{\boldsymbol{r}} \cdot \left[\frac{1+q}{q}\frac{1}{\gamma}\boldsymbol{F}P + \frac{1}{\gamma}f_{\mathrm{s}}\boldsymbol{p}P - \frac{1+q}{q}\frac{T}{\gamma}\nabla_{\boldsymbol{r}}P\right] \\ &-\omega\partial_\theta P + D_R\partial_\theta^2 P. \end{aligned} \tag{4}$$

Here, the symbol $\cdot$ represents a single contraction, $\nabla_{\boldsymbol{R}}$ and $\nabla_{\boldsymbol{r}}$ represent derivatives with respect to $\boldsymbol{R}$ and $\boldsymbol{r}$, and ∂_θ is the rotation operator in two dimensions.

We are interested in the spatial regions where the active–passive composite preferentially accumulates in the steady state. To this end, we attempt a coarse-grained description of our system at the mean-field level akin to the analysis in ref. 25 and 47–51, where we use the center of friction as a proxy for the position of the composite. This interpretation holds whenever the typical distance between the two particles is sufficiently small compared to the characteristic length scale of variation of the activity field. This gives us access to physically relevant fields such as the position density, orientation, *etc.* Particularly, we begin by performing a Cartesian multipole expansion of the probability density P in the eigenfunctions of the operator ∂_θ^2:[48]

$$P(\boldsymbol{R},\boldsymbol{r},\theta,t) = \phi + \boldsymbol{\sigma}\cdot\boldsymbol{p} + \boldsymbol{\mu}:(\boldsymbol{pp} - \mathbb{1}/2) + \boldsymbol{\Theta}(P), \tag{5}$$

where ϕ, $\boldsymbol{\sigma}$ and $\boldsymbol{\mu}$ are functions of $\boldsymbol{R}$ and $\boldsymbol{r}$, and : denotes a double contraction. Specifically, these correspond to the positional probability density, the average polarization, and the nematic tensor, respectively. The term $\boldsymbol{\Theta}(P)$ contains the dependencies on all the higher-order modes. Projecting eqn (4) onto the respective eigenfunctions, we obtain a hierarchy of time-evolution equations for the modes (ϕ, $\boldsymbol{\sigma}$, $\boldsymbol{\mu}$,...), details of which can be found in the ESI.† Importantly, we note that the slowest mode of the dynamics is the positional probability density $2\pi\phi(\boldsymbol{R},\boldsymbol{r},t) = \int \mathrm{d}\theta P(\boldsymbol{R},\boldsymbol{r},\theta,t)$, obtained by integrating out the rotational degree of freedom $\boldsymbol{p}$. In fact, $\phi(\boldsymbol{R},\boldsymbol{r},t)$ is a conserved quantity and satisfies a continuity equation:

$$\begin{aligned}\frac{\partial\phi}{\partial t} &= -\nabla_{\boldsymbol{R}}\cdot\left[-\frac{T}{\gamma}\frac{1}{1+q}\nabla_{\boldsymbol{R}}\phi + \frac{1}{1+q}\frac{1}{2\gamma}f_{\mathrm{s}}\boldsymbol{\sigma}\right] \\ &\quad -\nabla_{\boldsymbol{r}}\cdot\left[\frac{1}{2\gamma}f_{\mathrm{s}}\boldsymbol{\sigma} + \frac{1+q}{q}\frac{1}{\gamma}\boldsymbol{F}\phi - \frac{T}{\gamma}\frac{1+q}{q}\nabla_{\boldsymbol{r}}\phi\right].\end{aligned} \tag{6}$$

Additionally, the orientation field $\boldsymbol{\sigma}(\boldsymbol{R},\boldsymbol{r},t) = \int \mathrm{d}\theta \boldsymbol{p}P(\boldsymbol{R},\boldsymbol{r},\theta,t)$, which is related to the conditional average of the polarization vector $\boldsymbol{p}$ at fixed position of the active–passive composite, evolves in times as:

$$\begin{aligned}\frac{\partial\boldsymbol{\sigma}}{\partial t} &= -(D_R\mathbb{1} - \omega\varepsilon)\cdot\boldsymbol{\sigma} - \frac{1}{\gamma}\left(\frac{1}{1+q}\nabla_{\boldsymbol{R}} + \nabla_{\boldsymbol{r}}\right)(f_{\mathrm{s}}\phi) \\ &\quad -\frac{1}{\gamma}\frac{1+q}{q}\nabla_{\boldsymbol{r}}\cdot(\boldsymbol{F}\boldsymbol{\sigma}) + \mathcal{O}(\nabla_{\boldsymbol{R}}{}^2),\end{aligned} \tag{7}$$

where the dependence on the higher-order modes is captured in $\mathcal{O}(\nabla_{\boldsymbol{R}}{}^2)$. It is important to note that $\boldsymbol{\sigma}(\boldsymbol{R},\boldsymbol{r},t)$ is a fast mode due to the presence of the sink term $(D_R\mathbb{1} - \omega\varepsilon)\cdot\boldsymbol{\sigma} = \mathbb{L}^{-1}\boldsymbol{\sigma}$, where $\boldsymbol{\varepsilon}$ is the Levi-Civita tensor in two dimensions. The eigenvalues of the matrix $\mathbb{L}$ govern the decay-timescale of the orientation field $\boldsymbol{\sigma}$. This implies that $\boldsymbol{\sigma}$ can be approximated to be quasi-static at the timescale of variations in ϕ. Furthermore, we assume that the activity field is slowly varying in space, *i.e.*, the gradients of $f_{\mathrm{s}}(\boldsymbol{R})$ are (i) small compared to the persistence length of the chiral active particle, and (ii) small compared to the separation between the active and passive particles. This assumption implies that $\phi(\boldsymbol{R},\boldsymbol{r},t)$ also has small spatial variations, as well as, the contribution from the higher-order modes $\mathcal{O}(\nabla_{\boldsymbol{R}}{}^2)$ to eqn (7) can be neglected. The details of the coarse-graining and the validity of the approximation can be found in the ESI.†

The quasi-stationarity of $\boldsymbol{\sigma}(\boldsymbol{R},\boldsymbol{r},t)$, combined with the assumption of small spatial variations in the activity field, allows for the closure of the hierarchy of the system of equations without requiring information from higher-order modes. These are known as the adiabatic approximation and the small gradients approximation, respectively. Furthermore, we integrate out the bond coordinate $\boldsymbol{r}$ from the continuity equation in eqn (6) and derive an effective drift-diffusion equation for the probability density $\rho(\boldsymbol{R},t) = 2\pi\int \mathrm{d}\boldsymbol{r}\phi(\boldsymbol{R},\boldsymbol{r},t)$ of the collective coordinate of the active–passive composite:

$$\begin{aligned}\frac{\partial\rho(\boldsymbol{R},t)}{\partial t} &= -\nabla_{\boldsymbol{R}}\cdot\boldsymbol{J}, \\ &= -\nabla_{\boldsymbol{R}}\cdot[\boldsymbol{V}(\boldsymbol{R})\rho(\boldsymbol{R}) - \nabla_{\boldsymbol{R}}\cdot(\mathbb{D}(\boldsymbol{R})\rho(\boldsymbol{R}))].\end{aligned} \tag{8}$$

Here, the effective diffusion coefficient $\mathbb{D}(\boldsymbol{R})$ now depends on $\boldsymbol{R}$ and is given by:

$$\mathbb{D}(\boldsymbol{R}) = \frac{1}{1+q}\frac{T}{\gamma}\mathbb{1} + \frac{1}{(1+q)^2}\frac{1}{2\gamma^2}f_{\mathrm{s}}^2(\boldsymbol{R})\mathbb{L}^T. \tag{9}$$

Notably, $\mathbb{D}(\boldsymbol{R})$ has an antisymmetric part, which is a hallmark of odd-diffusive systems.[52–56] The effective drift $\boldsymbol{V}(\boldsymbol{R})$ can be written in terms of $\mathbb{D}(\boldsymbol{R})$ as:

$$\boldsymbol{V}(\boldsymbol{R}) = \left(\mathbb{1} - \frac{1}{2}\mathbb{L}[(1-q)\mathbb{1} + (1+q)\mathbb{B}]\mathbb{L}^{-1}\right)\nabla_{\boldsymbol{R}}\cdot\mathbb{D}(\boldsymbol{R}). \tag{10}$$

where the matrix $\mathbb{B}$ reads

$$\mathbb{B} = \frac{qk}{\gamma}\mathbb{L}\left(q\mathbb{1} + \frac{(1+q)k}{\gamma}\mathbb{L}\right)^{-1}. \tag{11}$$

We consider the activity field to vary only along the x-direction in the remainder of this study. Then, symmetry arguments dictate that the steady state density also varies only along the x coordinate. The stationary probability flux along this direction is then given by:

$$J_x(x) = -\frac{\epsilon}{2}\rho\partial_x\mathbb{D}_{xx} - \mathbb{D}_{xx}\partial_x\rho, \tag{12}$$

where $\mathbb{D}_{xx}$ denotes the xx element of the effective diffusion coefficient given in eqn (9). Furthermore, we show below that the quantity ϵ, which we call the *tactic parameter*, determines the accumulation behavior of the composite. Upon imposing a zero-flux condition along this direction, we obtain the steady state density:

$$\rho(x) \propto \left[1 + \frac{D_R}{D_R{}^2 + \omega^2}\frac{1}{1+q}\frac{1}{2\gamma T}f_{\mathrm{s}}^2(x)\right]^{-\epsilon/2}. \tag{13}$$

We find that the steady state density of our active–passive composite is determined by the sign of the exponent ϵ. When $\epsilon < 0(>0)$, $\rho(x)$ follows the same (opposite) trend as $f_{\mathrm{s}}(x)$, *i.e.*, the composite accumulates where the activity is high (low). As shown in the following, the tactic parameter depends on the interaction $\boldsymbol{F}$ between the chiral active particle and the passive

particle, the ratio of mobilities q and the chiral torque ω. Specifically, we consider two cases for the force $\boldsymbol{F}$ in our analytical treatment: force due to a spring with zero rest length and, force due to an infinitely stiff spring.

We first consider the case of a harmonic spring with zero rest length. In this case, the tactic parameter is given by the expression:

$$\epsilon = 1 - q\frac{(1+\Omega^2)(1+\tau)}{\Omega^2 + (1+\tau)^2}, \tag{14}$$

where we have introduced non-dimensional parameters

$$\begin{aligned} \Omega &= \omega\tau_{\mathrm{p}}, \\ \tau &= \frac{(1+q)k\tau_{\mathrm{p}}}{q\gamma}, \end{aligned} \tag{15}$$

which express the chiral torque and the spring relaxation time in units of the persistence time $\tau_{\mathrm{p}} = D_R^{-1}$ of the active particle due to rotational diffusion, respectively.

The steady state density given by eqn (13) and (14) is shown in Fig. 2, for the case of a sinusoidally varying activity field. The accumulation of the active–passive composite can be reversed from low-activity regions to high-activity regions by increasing the chiral torque Ω. In the limit of vanishing chiral torque, the tactic parameter (eqn (14)) reduces to

$$\lim_{\Omega\to 0} \epsilon = 1 - \frac{q}{1+\tau}, \tag{16}$$

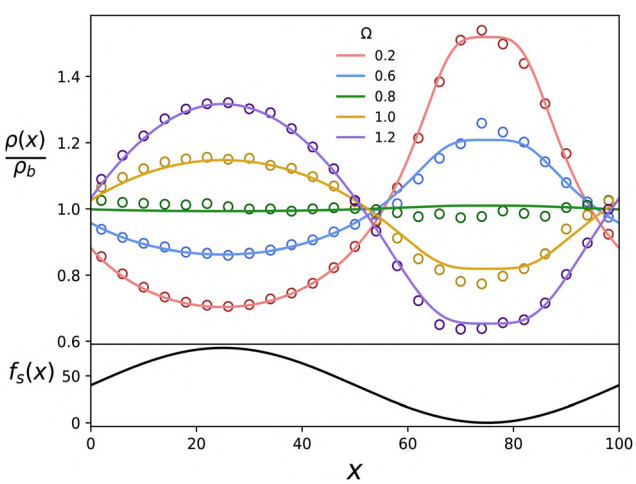

Fig. 2 Steady state density distribution (top panel) of the active–passive composites connected *via* a spring with $l_0 = 0$ for different chiral torques on the chiral active particle. The solid lines are plotted using the theoretical result (eqn (13) and (14)) and the symbols are obtained from Langevin dynamics simulations of eqn (1). The accumulation behavior of the composite is controlled by the intensity of the chiral torque Ω for a fixed size of the passive particle. The composite accumulates in regions of high-activity for rapidly spinning active particles and in regions of low-activity for slowly spinning active particles, respectively. The bottom panel shows the activity field $f_s(x) = 40[1 + \sin(2\pi x/L)]$ experienced by the chiral active particle. The y-axis in the top panel is normalized with the bulk density, defined as $\rho_b = 1/L$, where $L = 100$ is the simulation box size with periodic boundary conditions. The parameters of the simulation are $k_BT = 1.0$, $k = 14.0$, $\gamma = 1.0$, $D_R = 10.0$, $q = 2.0$, and the integration time step $\Delta t = D_R \times 10^{-5}$.

as previously reported in the study,[25] which focused on an active Brownian particle coupled to a passive particle. In this case, the passive particle has to be at least as large as the active particle ($q > 1$) for the composite to accumulate in high-activity regions. However, when the active particle experiences a chiral torque, even composites with a passive particle much smaller than the active particle ($q < 1$) can accumulate in high-activity regions, provided the chiral torque is sufficiently large. This finding is depicted in the left panel of Fig. 3. This indicates that the accumulation behavior of the active–passive composite can be tuned by applying a chiral torque to the active particle or by changing the size of the passive particle. We show this in the right panel of Fig. 3, where, for every value of the chiral torque, there exists a critical size of the passive particle beyond which the tactic behavior of the active–passive composite is reversed.

The preferential accumulation of the composite can be qualitatively understood as follows. Consider that the persistence time of the chiral active particle is smaller than the relaxation time of the spring connecting the two particles. The chiral active particle probes the neighborhood of the passive particle, locally sampling the activity gradients. This gives rise to a net pull on the passive particle towards the high-activity region. Since the persistence time of the active particle can be tuned *via* the chiral torque, *i.e.*, it becomes smaller than the spring relaxation time with increasing Ω, the tactic behavior of the composite can be switched from accumulation in low-activity regions to high-activity regions by increasing the chiral torque. It also follows that there is no tactic transition in the extreme case of $k \to \infty (\epsilon \to 1)$, in which case the spring relaxes instantaneously. This scenario corresponds to the chiral active particle and the passive particle being on top of each other.

Tuning the persistence time of the active particle *via* the chiral torque provides a handle on controlling the tactic behavior of composites. However, when fixing the distance between the chiral active particle and the passive particle *via* a rigid bond, the tactic behavior of the composite is independent of the persistence time and is determined by q alone. The tactic parameter (see ESI†) then reads

$$\epsilon = 1 - \frac{q}{2}, \tag{17}$$

same as reported in ref. 25 for two dimensions. This is shown in Fig. 4 for a sinusoidal variation of the activity field, where the transition in the accumulation behavior is obtained only by changing the ratio q.

To determine whether chemotaxis persists in the presence of excluded volume effects, we performed simulations of dimers where bonded particles interact *via* the Weeks–Chandler–Anderson (WCA) potential, given by $U_{\mathrm{WCA}}(r) = 4\varepsilon\left[\left(\frac{\sigma}{r}\right)^{12} - \left(\frac{\sigma}{r}\right)^{6}\right] + \varepsilon$ for $r \leq 2^{1/6}\sigma$, and $U_{\mathrm{WCA}}(r) = 0$ for $r > 2^{1/6}\sigma$. Here, ε represents the interaction strength, σ is the characteristic length scale of the interaction, and r denotes the center-to-center separation distance between two particles. We considered two cases: (1) where nonbonded interactions are absent and (2) where nonbonded particles also interact *via* the WCA potential.

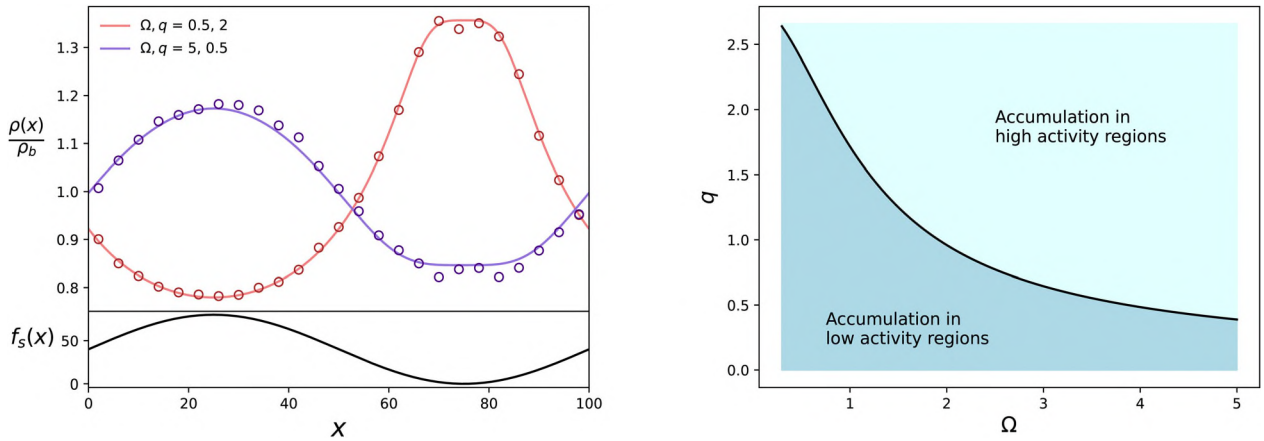

Fig. 3 Left: Comparison of steady state density distributions for the two extreme cases of the chiral torque Ω. In particular, when the chiral active particle is spinning slowly (red), and the passive particle is twice the size of the chiral active particle, the composite accumulates in low-activity regions. Whereas, when the chiral active particle is spinning extremely fast (purple), the composite accumulates in high-activity regions even for a passive particle half the size of the chiral active particle. The symbols represent simulations with the same parameters and the sinusoidal activity field as in Fig. 2. They are in excellent agreement with the theoretical predictions (solid lines). Right: State diagram in (q,Ω) for $\gamma D_r/k = 0.75$. The solid black curve represents the minimum size of the passive particle needed to reverse the accumulation behavior of the active–passive composite. Particularly at large values of the chiral torque, a small passive particle can facilitate this transition.

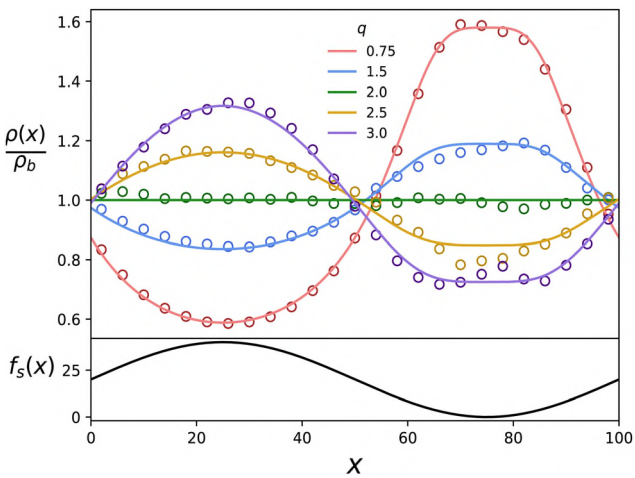

Fig. 4 Steady state density distribution (top panel) of the active–passive composites connected *via* an infinitely stiff spring for different sizes (q) of the passive particle. The solid lines are the analytical predictions (eqn (13) and (17)) and the symbols are obtained from Langevin dynamics simulations of eqn (1). Unlike in Fig. 2, the size of the passive particle determines the steady state accumulation: the composite accumulates in regions of high-activity for larger passive particles and in regions of low-activity for smaller passive particles respectively. The bottom panel shows the activity field $f_s(x) = 20[1 + \sin(2\pi x/L)]$ experienced by the chiral active particle. The y-axis in the top panel is normalized with the bulk density, defined as $\rho_b = 1/L$, where $L = 100$ is the simulation box size with periodic boundary conditions. The parameters of the simulation are $k_BT = 1.0$, $k = 500.0$, $\gamma = 1.0$, $D_R = 20.0$, $\Omega = 0.2$, $l_0 = 3.0$ and the integration time step $\Delta t = 5D_R \times 10^{-6}$.

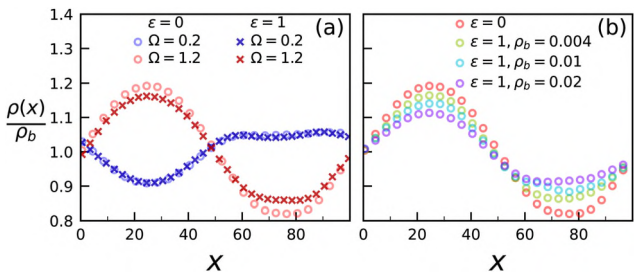

Fig. 5 The steady state density distribution of active–passive composites with $q = 2$ connected *via* a spring with $\ell_0 = 1.5$ and $k = 30$. The y-axis is normalized by the bulk density ρ_b. The sinusoidal activity field is the same as in Fig. 2, given by $f_s(x) = 20(1 + \sin(2\pi x/L))$. Panel (a) compares the results for case 1, where bonded particles interact *via* the WCA potential with $\varepsilon = 1$. For reference, results for fully noninteracting dimers (*i.e.*, neither bonded nor nonbonded interactions) with $\varepsilon = 0$ are also shown. The accumulation behavior of the composite is influenced by the strength of the chiral torque Ω. Panel (b) presents results for case 2, where, in addition to bonded interactions, nonbonded dimers also interact *via* the WCA potential ($\varepsilon = 1$). These results are compared with fully noninteracting dimers. The parameters of the simulation are $\Omega = 1.2$, $k_BT = 1.0$, $\gamma = 1.0$, $D_R = 10.0$, and the integration time step $\Delta t = 5D_R \times 10^{-6}$.

Fig. 5 presents the density profile along the x axis for dimers with $q = 2$, $k = 30$, and $\ell_0 = 1.5$. Panel (a) corresponds to case 1, where only bonded particles interact *via* the WCA potential. As expected, dimers with a chiral torque of $\Omega = 0.2$ on the active particle accumulate in low-activity regions, and including WCA interactions between bonded particles has no observable effects. In contrast, for $\Omega = 1.2$, where dimers accumulate in the high-activity regions, introducing WCA interactions between bonded particles slightly reduces the chemotactic response. Panel (b) presents the results for case 2. In the dilute limit, chemotaxis remains robust, with dimers accumulating in high-activity regions. As the bulk density increases, particle collisions lead to reorientations, which consequently reduce the accumulation in the high-activity regions slightly.

III. Conclusion & outlook

Directed motion toward regions of high concentration is a defining feature of living systems, spanning length scales from protein complexes to bacteria. In this work, we demonstrate that a minimal model system composed of a chiral active particle coupled to a passive particle, can exhibit preferential accumulation as an emergent property. Particularly, when the chiral active particle and the passive particle are connected by a rigid rod, the transition from accumulation in low-activity regions to high-activity regions depends solely on the size of the passive particle, similar to the previous studies.[25,47] In contrast, when the coupling is mediated by a harmonic spring of zero rest length, the crossover is determined by the chiral torque. Additionally, we observe that this preferential accumulation is possible even when the chiral active particle is coupled to a small passive particle, provided the chiral torque is sufficiently large, which deviates from previous findings. Our results demonstrate that even when excluded volume effects are considered, accumulation in high-activity regions remains robust in the dilute limit, further underscoring the effect of chirality as a control parameter. The mechanism underlying the preferential accumulation involves the anchoring effect of the passive particle, which allows the chiral active particle to explore the activity gradients and leads to the composite effectively drifting up the gradient. Moreover, our results show that when chiral active particles are connected into chains, they accumulate in high-activity regions at sufficiently high Ω for chain lengths exceeding three monomers (*cf.* Fig. SI 1 of the ESI†). Previous theoretical studies suggested that directed motion can emerge when two chiral active particles with equal and opposite torques are coupled, creating a tug-of-war effect.[48] In contrast, we show that dimers with the same torque direction experience a cumulative chiral effect that suppresses chemotaxis, even at very high chiral torques. This can be attributed to the reduction of the persistence time of the active monomers in the presence of chirality, in which case short chains preferentially accumulate in low activity regions.[27]

Chiral active matter is ubiquitous in nature, where chiral symmetry breaking at the cellular and subcellular levels contributes to bilateral asymmetry in organisms, organs, and tissues.[57–61] At the cellular scale, active torques generated by the actomyosin cytoskeleton induce chiral symmetry breaking,[62] while membrane-anchored motor proteins produce rotational forces that drive flagellar motion and cell propulsion.[32,63] Beyond biological systems, chirality plays a crucial role in practical applications, enabling functionalities such as particle sorting[64–66] and synchronization.[67,68] At the millimeter scale, vibrots provide a well-controlled experimental platform for studying chiral active matter,[69–73] with tunable chiral torques achieved through bristle configurations. These systems can also be assembled into polymeric chains connected by springs.[74] Chiral active granular particles have similarly been realized by breaking translational symmetry.[75,76] At the microscale, recent experiments have shown that amoeboid cell motility can be enhanced by coupling them to passive beads.[77] Our results offer a theoretical framework that can be tested in experimental systems where chirality emerges from symmetry breaking in body shape or self-propulsion mechanisms. Possible microscale realizations include active colloids, such as L-shaped particles confined using optical tweezers, or catalysis-coated synthetic swimmers.[3,4,78] Advances in fabrication techniques, such as glancing angle metal evaporation, now allow precise control over the spin rates of catalytic Janus swimmers, enabling systematic investigations of chiral active dynamics.[78]

Our model does not account for the hydrodynamic interactions between the active–passive composite with the surrounding solvent, a class of models known as dry active matter models.[3] An intriguing extension of this work would involve incorporating hydrodynamic effects into the modeling, which we delegate to future studies.

Data availability

The code for calculating the steady state positional probability density of the active–passive composite can be found at **https://doi.org/10.5281/zenodo.14883803** with DOI – **https://doi.org/10.5281/zenodo.14883803**. The version of the code employed for this study is version v1.0.1.

Conflicts of interest

There are no conflicts to declare.

Acknowledgements

A. S. acknowledges support by the Deutsche Forschungsgemeinschaft (DFG) within Project No. SH 1275/5-1. J. U. S. thanks the cluster of excellence ''Physics of Life'' at TU Dresden supported by Deutsche Forschungsgemeinschaft (DFG) under Germany's excellence strategy - EXC 2068 - 390729961. B. V. thanks S. Ravichandir for fruitful discussions, and A. Pandit for assistance in designing the schematic.

References

1 P. Hänggi and F. Marchesoni, Artificial Brownian motors: Controlling transport on the nanoscale, *Rev. Mod. Phys.*, 2009, **81**(1), 387–442, DOI: **10.1103/RevModPhys.81.387**.

2 S. Ramaswamy, The Mechanics and Statistics of Active Matter, *Annu. Rev. Condens. Matter Phys.*, 2010, **1**(1), 323–345.

3 M. C. Marchetti, J. F. Joanny, S. Ramaswamy, T. B. Liverpool, J. Prost and M. Rao, *et al.*, Hydrodynamics of soft active matter, *Rev. Mod. Phys.*, 2013, **85**(3), 1143–1189, DOI: **10.1103/RevModPhys.85.1143**.

4 C. Bechinger, R. Di Leonardo, H. Löwen, C. Reichhardt, G. Volpe and G. Volpe, Active particles in complex and crowded environments, *Rev. Mod. Phys.*, 2016, **88**(4), 045006, DOI: **10.1103/RevModPhys.88.045006**.

5 S. Ramaswamy, Active matter, *J. Stat. Mech.*, 2017, **2017**(5), 054002, DOI: **10.1088/1742-5468/aa6bc5**.

6 *E. coli in Motion. Biological and Medical Physics, Biomedical Engineering*, ed. H. C. Berg, Springer, New York, NY, 2004. **https://link.springer.com/10.1007/b97370**.
7 M. E. Cates, Diffusive transport without detailed balance in motile bacteria: does microbiology need statistical physics?, *Rep. Prog. Phys.*, 2012, **75**(4), 042601, DOI: **10.1088/0034-4885/75/4/042601**.
8 J. A. Kromer, N. de la Cruz and B. M. Friedrich, Chemokinetic Scattering, Trapping, and Avoidance of Active Brownian Particles, *Phys. Rev. Lett.*, 2020, **124**(11), 118101, DOI: **10.1103/PhysRevLett.124.118101**.
9 J. R. Howse, R. A. L. Jones, A. J. Ryan, T. Gough, R. Vafabakhsh and R. Golestanian, Self-Motile Colloidal Particles: From Directed Propulsion to Random Walk, *Phys. Rev. Lett.*, 2007, **99**(4), 048102, DOI: **10.1103/PhysRevLett.99.048102**.
10 G. S. Fraenkel and D. L. Gunn, The Orientation of Animals, Kinesis, Taxes and Compass Reactions, *Ann. Entomol. Soc. Am.*, 1941, **34**(3), 690, DOI: **10.1093/aesa/34.3.690a**.
11 M. J. Schnitzer, Theory of continuum random walks and application to chemotaxis, *Phys. Rev. B: Condens. Matter Mater. Phys.*, 1993, **48**(4), 2553–2568, DOI: **10.1103/PhysRevE.48.2553**.
12 A. Sharma and J. M. Brader, Brownian systems with spatially inhomogeneous activity, *Phys. Rev. E*, 2017, **96**(3), 032604, DOI: **10.1103/PhysRevE.96.032604**.
13 L. Caprini, U. M. B. Marconi, R. Wittmann and H. Löwen, Dynamics of active particles with space-dependent swim velocity, *Soft Matter*, 2022, **18**(7), 1412–1422.
14 E. F. Keller and L. A. Segel, Model for chemotaxis, *J. Theor. Biol.*, 1971, **30**(2), 225–234.
15 B. Liebchen and H. Löwen, Synthetic Chemotaxis and Collective Behavior in Active Matter, *Acc. Chem. Res.*, 2018, **51**(12), 2982–2990, DOI: **10.1021/acs.accounts.8b00215**.
16 H. Stark, Artificial Chemotaxis of Self-Phoretic Active Colloids: Collective Behavior, *Acc. Chem. Res.*, 2018, **51**(11), 2681–2688, DOI: **10.1021/acs.accounts.8b00259**.
17 B. Qian, D. Montiel, A. Bregulla, F. Cichos and H. Yang, Harnessing thermal fluctuations for purposeful activities: the manipulation of single micro-swimmers by adaptive photon nudging, *Chem. Sci.*, 2013, **4**(4), 1420–1429.
18 T. Mano, J. B. Delfau, J. Iwasawa and M. Sano, Optimal run-and-tumble–based transportation of a Janus particle with active steering, *Proc. Natl. Acad. Sci. U. S. A.*, 2017, **114**(13), E2580–E2589.
19 H. Massana-Cid, C. Maggi, G. Frangipane and R. Di Leonardo, Rectification and confinement of photokinetic bacteria in an optical feedback loop, *Nat. Commun.*, 2022, **13**(1), 2740.
20 C. Lozano, B. ten Hagen, H. Löwen and C. Bechinger, Phototaxis of synthetic microswimmers in optical landscapes, *Nat. Commun.*, 2016, **7**(1), 12828.
21 C. Lozano and C. Bechinger, Diffusing wave paradox of phototactic particles in traveling light pulses, *Nat. Commun.*, 2019, **10**(1), 2495.
22 F. Martinez-Pedrero and P. Tierno, Magnetic Propulsion of Self-Assembled Colloidal Carpets: Efficient Cargo Transport *via* a Conveyor-Belt Effect, *Phys. Rev. Appl.*, 2015, **3**(5), 051003, DOI: **10.1103/PhysRevApplied.3.051003**.
23 A. Geiseler, P. Hänggi and F. Marchesoni, Self-Polarizing Microswimmers in Active Density Waves, *Sci. Rep.*, 2017, **7**(1), 41884.
24 A. Geiseler, P. Hänggi, F. Marchesoni, C. Mulhern and S. Savel'ev, Chemotaxis of artificial microswimmers in active density waves, *Phys. Rev. E*, 2016, **94**(1), 012613, DOI: **10.1103/PhysRevE.94.012613**.
25 H. D. Vuijk, H. Merlitz, M. Lang, A. Sharma and J. U. Sommer, Chemotaxis of Cargo-Carrying Self-Propelled Particles, *Phys. Rev. Lett.*, 2021, **126**(20), 208102, DOI: **10.1103/PhysRevLett.126.208102**.
26 H. D. Vuijk, S. Klempahn, H. Merlitz, J. U. Sommer and A. Sharma, Active colloidal molecules in activity gradients, *Phys. Rev. E*, 2022, **106**(1), 014617, DOI: **10.1103/PhysRevE.106.014617**.
27 P. L. Muzzeddu, A. Gambassi, J. U. Sommer and A. Sharma, Migration and Separation of Polymers in Nonuniform Active Baths, *Phys. Rev. Lett.*, 2024, **133**(11), 118102, DOI: **10.1103/PhysRevLett.133.118102**.
28 B. Liebchen and D. Levis, Chiral active matter, *EPL*, 2022, **139**(6), 67001, DOI: **10.1209/0295-5075/ac8f69**.
29 H. Löwen, Chirality in microswimmer motion: From circle swimmers to active turbulence, *Eur. Phys. J.-Spec. Top.*, 2016, **225**(11), 2319–2331, DOI: **10.1140/epjst/e2016-60054-6**.
30 H. C. Crenshaw, A New Look at Locomotion in Microorganisms: Rotating and Translating1, *Am. Zool.*, 1996, **36**(6), 608–618, DOI: **10.1093/icb/36.6.608**.
31 E. Lauga, W. R. DiLuzio, G. M. Whitesides and H. A. Stone, Swimming in Circles: Motion of Bacteria near Solid Boundaries, *Biophys. J.*, 2006, **90**(2), 400–412.
32 I. H. Riedel, K. Kruse and J. Howard, A Self-Organized Vortex Array of Hydrodynamically Entrained Sperm Cells, *Science*, 2005, **309**(5732), 300–303, DOI: **10.1126/science.1110329**.
33 B. M. Friedrich and F. Jülicher, Chemotaxis of sperm cells, *Proc. Natl. Acad. Sci. U. S. A.*, 2007, **104**(33), 13256–13261, DOI: **10.1073/pnas.0703530104**.
34 K. Drescher, K. C. Leptos, I. Tuval, T. Ishikawa, T. J. Pedley and R. E. Goldstein, Dancing Volvox: Hydrodynamic Bound States of Swimming Algae, *Phys. Rev. Lett.*, 2009, **102**(16), 168101, DOI: **10.1103/PhysRevLett.102.168101**.
35 F. Kümmel, B. ten Hagen, R. Wittkowski, I. Buttinoni, R. Eichhorn and G. Volpe, *et al.*, Circular Motion of Asymmetric Self-Propelling Particles, *Phys. Rev. Lett.*, 2013, **110**(19), 198302, DOI: **10.1103/PhysRevLett.110.198302**.
36 D. Matsunaga, J. K. Hamilton, F. Meng, N. Bukin, E. L. Martin and F. Y. Ogrin, *et al.*, Controlling collective rotational patterns of magnetic rotors, *Nat. Commun.*, 2019, **10**(1), 4696.
37 P. Arora, A. K. Sood and R. Ganapathy, Emergent stereoselective interactions and self-recognition in polar chiral active ellipsoids, *Sci. Adv.*, 2021, **7**(9), eabd0331, DOI: **10.1126/sciadv.abd0331**.
38 E. S. Bililign, F. Balboa Usabiaga, Y. A. Ganan, A. Poncet, V. Soni and S. Magkiriadou, *et al.*, Motile dislocations knead odd crystals into whorls, *Nat. Phys.*, 2022, **18**(2), 212–218.

39 L. Caprini and U. M. B. Marconi, Active chiral particles under confinement: surface currents and bulk accumulation phenomena, *Soft Matter*, 2019, **15**(12), 2627–2637.
40 Q. L. Lei, M. P. Ciamarra and R. Ni, Nonequilibrium strongly hyperuniform fluids of circle active particles with large local density fluctuations, *Sci. Adv.*, 2019, **5**(1), eaau7423, DOI: **10.1126/sciadv.aau7423**.
41 U. M. B. Marconi and L. Caprini, Spontaneous generation of angular momentum in chiral active crystals, *Soft Matter*, 2025, **21**, 2586–2606, DOI: **10.1039/D4SM01426J**.
42 B. Ventejou, H. Chaté, R. Montagne and X. Shi, Susceptibility of Orientationally Ordered Active Matter to Chirality Disorder, *Phys. Rev. Lett.*, 2021, **127**(23), 238001, DOI: **10.1103/PhysRevLett.127.238001**.
43 A. Souslov, B. C. Van Zuiden, D. Bartolo and V. Vitelli, Topological sound in active-liquid metamaterials, *Nat. Phys.*, 2017, **13**(11), 1091–1094.
44 Z. Dunajova, B. P. Mateu, P. Radler, K. Lim, D. Brandis and P. Velicky, *et al.*, Chiral and nematic phases of flexible active filaments, *Nat. Phys.*, 2023, **19**(12), 1916–1926.
45 H. Shi, D. A. Quint, G. M. Grason, A. Gopinathan and K. C. Huang, Chiral twisting in a bacterial cytoskeletal polymer affects filament size and orientation, *Nat. Commun.*, 2020, **11**(1), 1408.
46 H. Risken, Springer Series in Synergetics, in *The Fokker-Planck Equation: Methods of Solution and Applications*. ed., H. Haken, Springer, Berlin, Heidelberg, 1996, vol. 18, **https://link.springer.com/10.1007/978-3-642-61544-3**.
47 P. L. Muzzeddu, É. Roldán, A. Gambassi and A. Sharma, Taxis of cargo-carrying microswimmers in traveling activity waves(a), *EPL*, 2023, **142**(6), 67001, DOI: **10.1209/0295-5075/acd8e9**.
48 P. L. Muzzeddu, H. D. Vuijk, H. Löwen, J. U. Sommer and A. Sharma, Active chiral molecules in activity gradients, *J. Chem. Phys.*, 2022, **157**(13), 134902, DOI: **10.1063/5.0109817**.
49 M. E. Cates and J. Tailleur, When are active Brownian particles and run-and-tumble particles equivalent? Consequences for motility-induced phase separation, *EPL*, 2013, **101**(2), 20010, DOI: **10.1209/0295-5075/101/20010**.
50 A. P. Solon, M. E. Cates and J. Tailleur, Active brownian particles and run-and-tumble particles: A comparative study, *Eur. Phys. J.-Spec. Top.*, 2015, **224**(7), 1231–1262, DOI: **10.1140/epjst/e2015-02457-0**.
51 T. Adeleke-Larodo, *Non-equilibrium dynamics of active enzymes*, Doctoral thesis, University of Oxford, 2020, **https://ora.ox.ac.uk/objects/uuid:fcc43663-0ced-406b-8291-50999f912eff**.
52 C. Hargus, J. M. Epstein and K. K. Mandadapu, Odd Diffusivity of Chiral Random Motion, *Phys. Rev. Lett.*, 2021, **127**(17), 178001, DOI: **10.1103/PhysRevLett.127.178001**.
53 E. Kalz, H. D. Vuijk, I. Abdoli, J. U. Sommer, H. Löwen and A. Sharma, Collisions Enhance Self-Diffusion in Odd-Diffusive Systems, *Phys. Rev. Lett.*, 2022, **129**(9), 090601, DOI: **10.1103/PhysRevLett.129.090601**.
54 E. Kalz, H. D. Vuijk, J. U. Sommer, R. Metzler and A. Sharma, Oscillatory Force Autocorrelations in Equilibrium Odd-Diffusive Systems, *Phys. Rev. Lett.*, 2024, **132**(5), 057102, DOI: **10.1103/PhysRevLett.132.057102**.
55 C. Hargus, A. Deshpande, A. K. Omar and K. K. Mandadapu, Flux Hypothesis for Odd Transport Phenomena, *Phys. Rev. Lett.*, 2025, **134**(9), 097105, DOI: **10.1103/PhysRevLett.134.097105**.
56 E. Kalz, A. Sharma and R. Metzler, Field theory of active chiral hard disks: a first-principles approach to steric interactions, *J. Phys. A: Math. Theor.*, 2024, **57**(26), 265002, DOI: **10.1088/1751-8121/ad5089**.
57 T. Hayashi and R. Murakami, Left-right asymmetry in Drosophila melanogaster gut development, *Dev., Growth Differ.*, 2001, **43**(3), 239–246.
58 Y. Shibazaki, M. Shimizu and R. Kuroda, Body handedness is directed by genetically determined cytoskeletal dynamics in the early embryo, *Curr. Biol.*, 2004, **14**(16), 1462–1467.
59 K. C. Huang, D. W. Ehrhardt and J. W. Shaevitz, The molecular origins of chiral growth in walled cells, *Curr. Opin. Microbiol.*, 2012, **15**(6), 707–714.
60 K. Taniguchi, R. Maeda, T. Ando, T. Okumura, N. Nakazawa and R. Hatori, *et al.*, Chirality in planar cell shape contributes to left-right asymmetric epithelial morphogenesis, *Science*, 2011, **333**(6040), 339–341.
61 T. Savin, N. A. Kurpios, A. E. Shyer, P. Florescu, H. Liang and L. Mahadevan, *et al.*, On the growth and form of the gut, *Nature*, 2011, **476**(7358), 57–62.
62 S. R. Naganathan, S. Fürthauer, M. Nishikawa, F. Jülicher and S. W. Grill, Active torque generation by the actomyosin cell cortex drives left-right symmetry breaking, *eLife*, 2014, **3**, e04165.
63 E. M. Purcell, The efficiency of propulsion by a rotating flagellum, *Proc. Natl. Acad. Sci. U. S. A.*, 1997, **94**(21), 11307–11311.
64 M. Mijalkov and G. Volpe, Sorting of chiral microswimmers, *Soft Matter*, 2013, **9**(28), 6376–6381.
65 J. Su, H. Jiang and Z. Hou, Disordered hyperuniform obstacles enhance sorting of dynamically chiral microswimmers, *Soft Matter*, 2019, **15**(34), 6830–6835.
66 Li. T. C. Xu Gh and Ai Bq, Sorting of chiral active particles by a spiral shaped obstacle, *Phys. A Stat. Mech. Appl.*, 2022, **608**, 128247.
67 D. Levis, I. Pagonabarraga and B. Liebchen, Activity induced synchronization: Mutual flocking and chiral self-sorting, *Phys. Rev. Res.*, 2019, **1**(2), 023026.
68 S. Samatas and J. Lintuvuori, Hydrodynamic synchronization of chiral microswimmers, *Phys. Rev. Lett.*, 2023, **130**(2), 024001.
69 E. Altshuler, J. M. Pastor, A. Garcimartín, I. Zuriguel and D. Maza, Vibrot, a Simple Device for the Conversion of Vibration into Rotation Mediated by Friction: Preliminary Evaluation, *PLoS One*, 2013, **8**(8), e67838.
70 C. Scholz, S. D'Silva and T. Pöschel, Ratcheting and tumbling motion of Vibrots, *New J. Phys.*, 2016, **18**(12), 123001, DOI: **10.1088/1367-2630/18/12/123001**.
71 C. Scholz and T. Pöschel, Velocity Distribution of a Homogeneously Driven Two-Dimensional Granular Gas, *Phys. Rev.*

Lett., 2017, **118**(19), 198003, DOI: **10.1103/PhysRevLett.118.198003**.

72 M. Broseghini, C. Ceccolini, C. D. Volpe and S. Siboni, The Notched Stick, an ancient vibrot example, *PLoS One*, 2019, **14**(6), e0218666.

73 C. Scholz, M. Engel and T. Pöschel, Rotating robots move collectively and self-organize, *Nat. Commun.*, 2018, **9**(1), 931.

74 C. Scholz, A. Ldov, T. Pöschel, M. Engel and H. Löwen, Surfactants and rotelles in active chiral fluids, *Sci. Adv.*, 2021, **7**(16), eabf8998, DOI: **10.1126/sciadv.abf8998**.

75 O. Dauchot and V. Démery, Dynamics of a self-propelled particle in a harmonic trap, *Phys. Rev. Lett.*, 2019, **122**(6), 068002.

76 K. Engbring, D. Boriskovsky, Y. Roichman and B. Lindner, A nonlinear fluctuation-dissipation test for Markovian systems, *Phys. Rev. X*, 2023, **13**(2), 021034.

77 V. Lepro, R. Großmann, S. Sharifi Panah, O. Nagel, S. Klumpp and R. Lipowsky, *et al.*, Optimal Cargo Size for Active Diffusion of Biohybrid Microcarriers, *Phys. Rev. Appl.*, 2022, **18**(3), 034014, DOI: **10.1103/PhysRevApplied.18.034014**.

78 R. Archer, A. Campbell and S. Ebbens, Glancing angle metal evaporation synthesis of catalytic swimming Janus colloids with well defined angular velocity, *Soft Matter*, 2015, **11**(34), 6872–6880.